

David W. Fellows¹

Mem. ASME

Department of Aerospace Engineering,
University of Illinois at Urbana-Champaign,
Urbana-Champaign, IL 61801
e-mail: dfellow2@illinois.edu

Vincent Iskandar

Department of Aerospace Engineering,
University of Illinois at Urbana-Champaign,
Urbana-Champaign, IL 61801
e-mail: vi5@illinois.edu

Daniel J. Bodony

Blue Waters Professor

Department of Aerospace Engineering,
University of Illinois at Urbana-Champaign,
Urbana-Champaign, IL 61801
e-mail: bodony@illinois.edu

Ryan C. McGowan

Mem. ASME

DEVCOM Army Research Laboratory,
Aberdeen Proving Ground, MD 21005
e-mail: ryan.c.mcgowan3.civ@army.mil

Sang-Guk Kang

Mem. ASME

DEVCOM Army Research Laboratory,
Aberdeen Proving Ground, MD 21005
e-mail: sangguk.s.kang.civ@army.mil

Aaron J. Pope

Mem. ASME

DEVCOM Army Research Laboratory,
Aberdeen Proving Ground, MD 21005
e-mail: aaron.j.pope7.civ@army.mil

Chol-Bum M. Kweon

VICTOR ERP,

DEVCOM Army Research Laboratory,
Aberdeen Proving Ground, MD 21005
e-mail: chol-bum.m.kweon2.civ@army.mil

A Method for Predicting the Aeroelastic Response of Radial Turbomachines

Aircraft intermittent combustion engines often incorporate turbochargers adapted from ground-based applications to improve their efficiency and performance. These turbochargers can operate at off-design conditions and experience blade failures brought on by aerodynamic-induced blade resonances. A reduced-order model of the aeroelastic response of general fluid–structural configurations is developed using the Euler–Lagrange equation informed by numerical data from uncoupled computational fluid dynamic (CFD) and computational structural dynamic calculations. The structural response is derived from a method of assumed-modes approach. The unsteady fluid response is described by a modified version of piston theory that approximates the local transient pressure fluctuation in conjunction with steady CFD solution data. The reduced-order model is first applied to a classical panel flutter scenario and found to predict a flutter boundary that compares favorably to the boundary identified by existing theory and experimental data. The model is then applied to the high-pressure turbine of a dual-stage turbocharger. The model predictions are shown to reliably determine the lack of turbine blade flutter and rudimentary damping comparisons are performed to assess the ability of the model to ascertain the susceptibility of the turbine to forced response. Obstacles associated with the current experimental state of the art that impinge upon further numerical validation are discussed.

[DOI: 10.1115/1.4057062]

Keywords: aeromechanical instabilities, computational fluid dynamics (CFD), fluid dynamics and heat transfer phenomena in compressor and turbine components of gas turbine engines, turbine blade and measurement advancements

1 Introduction

The development and use of small aircraft is attractive because they offer improved versatility compared to conventional aircraft, especially in applications such as reconnaissance, aerial photography, and telecommunications [1]. The increased utilization of these vehicles has illuminated the challenges of designing and developing sophisticated propulsion systems needed to sustain operation at altitude. Difficulties associated with operating in this environment include the need for turbomachinery to pressurize the engine intake due to low air density and the need for improved power output required to fly at the speeds necessary to provide sufficient lift [2]. For some applications, turbocharged intermittent combustion engines are favored over gas turbine engines because

the resulting aircraft is lighter [3], more fuel efficient [4,5], and has a more favorable power-to-weight ratio [6]. However, turbocharger manufacturers have not yet broadly embraced the aviation industry, and consequently these devices are frequently required to operate outside of their automotive-designed operating envelopes. At the operating conditions encountered during flight, the turbocharger may operate at rotational speeds exceeding 100,000 revolutions per minute, exposing the turbine blades to extreme thermal and mechanical stresses over prolonged periods of time [7]. The device is thus prone to a variety of fluid–structural interactions that may induce high-cycle fatigue of the turbine blades [8].

Two of the most relevant fluid–structural interactions impacting the lifetime of radial turbine blades within aircraft turbochargers are flutter and forced response (alternatively referred to as resonant vibration). Flutter is an unstable, self-excited vibration in which energy is extracted from the flow by the deformation of the structure. This phenomenon is notably difficult to predict as it may occur over a wide range of speeds and reduced frequencies [9]. Past investigations of flutter in turbomachinery have identified that various factors influence flutter onset, including device inlet

¹Corresponding author.

Contributed by the International Gas Turbine Institute (IGTI) of ASME for publication in the JOURNAL OF TURBOMACHINERY. Manuscript received June 27, 2022; final manuscript received February 28, 2023; published online April 3, 2023. Assoc. Editor: Lorenzo Mazzei.

This work is in part a work of the U.S. Government. ASME disclaims all interest in the U.S. Government's contributions.

pressure [10], blade reduced frequency [11,12], and blade mode shape [13].

Forced response occurs when the blades encounter an external forcing at a frequency that is an integer multiple of one of the natural frequencies of the blade, resulting in significant deflection amplitudes. These external forces can come from several sources including inlet flow distortions [14], wake excitations [15], rotor–stator interactions [16], and leakage flows [17]. The ideal method of avoiding forced response is to modify the blade geometry such that the natural frequencies of problematic mode shapes lie above the forcing frequencies [18], but this design criterion becomes difficult to adhere to as the turbomachine operates at high rotational speeds. Forced response in turbomachinery is very difficult to avoid [19] and so specific attention is given toward damping the response. The overall damping in turbomachinery applications originates from material, mechanical and aerodynamic mechanisms. Material damping is often negligible for turbomachinery materials of interest and design practices frequently choose to minimize the mechanical damping, leaving aerodynamic damping as the most effective method to avoid the build up of structural energy associated with unsteady external forcing [20]. Whereas material and mechanical damping can be intentionally influenced by the designer, aerodynamic damping cannot [21]. Accurately estimating the aerodynamic damping thus becomes an important facet of mitigating forced response phenomena, as well as to identify conditions at which aerodynamic mechanisms can serve to excite the structure and induce flutter.

The utilization of experimental techniques to assess the susceptibility of a turbomachine to flutter and forced response has long been successful, and many techniques exist to assess the fluid and structural behavior of turbomachinery during operation [2]. However, these techniques have been developed for use with large, axial turbomachines and are often ineffective toward investigating the compact, radial turbomachinery prominent in aircraft turbocharger designs. The small size of these devices makes it difficult to install multiple measurement probes into the device, limiting the type and amount of data that can be measured through experiment. Additionally, the instrumentation available is often unable to survive the high-speed, high-temperature turbine operating environment. Most importantly, experimental investigations are time consuming, making the potential need to investigate multiple operating conditions prohibitive.

The use of experiment as a design analysis tool has largely been superseded by numerical investigation methods, of which several computational methods have been developed. The most accurate numerical investigations calculate the fluid–structural dynamic behavior of the device via fully coupled simulations in which the fluid and structural governing equations are solved simultaneously. The specific choice of fluid and structural equations considered in the analysis has varied significantly. Bréard et al. [22] coupled a three-dimensional nonlinear, viscous, unsteady representation of the fluid to a three-dimensional linear modal model of the structure to successfully predict the forced response of a low aspect-ratio transonic fan. A similar fluid–structural model was additionally employed by Vahdati and Imregun [23] to predict the aeroelastic behavior of the NASA Rotor 67 fan blade at peak efficiency and near-stall conditions. Fully coupled simulations with simplified fluid representations have also proven effective; for one, Green and Marshall [24] coupled a three-dimensional linearized, inviscid, unsteady flow solver to a three-dimensional nonlinear, transient structural finite element solver to predict turbomachinery forced vibration.

The major disadvantage of fully coupled prediction methods lies in the numerical expense associated with discretizing the fluid and structural governing equations [25]. A series of decoupled prediction methods where the fluid and structural responses are considered independent have since been developed with encouraging results. Dickmann et al. [26] utilized a transient fluid simulation of a turbocharger centrifugal compressor to acquire the unsteady pressure solution on the impeller blades. The pressure data were then

transformed into the frequency domain and the complex modal pressure data were applied to a finite element model of the impeller. A comparison against experimental data suggests that the decoupled method can sufficiently predict the vibration behavior of the structure. Chiang and Kielb [19] developed a decoupled method where the flow excitation sources were computed using multiple models. Wake excitations were computed by a semi-empirical wake/vortex model, inlet distortion effects were modeled from measured data, and pressure disturbances were obtained from a quasi-three-dimensional Euler solution. The unsteady aerodynamic modal forces and aerodynamic damping were then computed in conjunction with a three-dimensional, linear finite element model of the structure. The method was capable of predicting the presence of resonant vibration in an axial fan and an axial supersonic turbine. Finally, Moffatt et al. [25] identified that the computational intensity associated with the fluid solution could be further reduced by solving the fluid equations in the spectral domain. Their method solved the three-dimensional Navier–Stokes equations in conjunction with a three-dimensional linear finite element representation of the structure, and the forced response predictions from the analysis compared well with strain gauge test data.

The decoupled simulation methods suggest that reduced-order aeroelastic calculations can provide accurate predictions of the blade dynamics in axial turbomachines. This work describes a decoupled aeroelastic prediction method that differs from the existing methods in that it utilizes a modified form of piston theory where the unsteady fluid response is derived in conjunction with steady flow solution data to model the aerodynamic response to deformation of the structure. The steady flow solution method further lowers the computational complexity of the model in comparison to the decoupled prediction methods discussed previously. Furthermore, the method discussed here is additionally applied to radial turbomachinery that has not been well investigated by previous numerical methods.

2 Reduced-Order Model Derivation

The reduced-order modeling method developed in this work utilizes the Euler–Lagrange equation in conjunction with an assumed-modes method to derive equations of motion for the structure in consideration. The process of describing the reduced fluid and structural responses is described in the following subsections and followed by the procedure to predict the flutter boundary and the presence of forced response in a given fluid–structural configuration.

2.1 Euler–Lagrange Equation. A general, three-dimensional structure with domain Ω and bounding surface S is considered as the system of interest. The bounding surface is in full or partial contact with a surrounding fluid domain. The deformation of this structure is prescribed in terms of a set of specified shape functions, $\vec{\psi}_j$, each with a relative amplitude described through a set of generalized coordinates, q_j . The approximation of the structural deformation is defined as

$$\vec{u}(\vec{x}, t) = \sum_{j=1}^{N_m} q_j(t) \vec{\psi}_j(\vec{x}) \quad (1)$$

where N_m is the number of modes used to construct the reduced structural response. The Euler–Lagrange equation [27] is used to derive the equations of motion governing the dynamics of this system from a conservation of energy perspective. The Euler–Lagrange equation provides a differential equation governing the j th generalized coordinate defined as

$$\frac{d}{dt} \left(\frac{\partial T}{\partial \dot{q}_j} \right) - \frac{\partial T}{\partial q_j} + \frac{\partial U}{\partial q_j} = \frac{d(\delta W)}{d(\delta q_j)} \quad (2)$$

The left-hand side terms of Eq. (2) describe the energy associated with the deformation of the structure in modes associated with each generalized coordinate. These terms include changes in the kinetic energy and strain energy of the structure. The terms on the right-hand side of Eq. (2) describe the unsteady work performed on the structure by fluid forces deforming the structure in each mode shape. The intrinsic dissipation term has been neglected as the fluid–structural systems of interest to this work encounter low amplitude deformation at modest temperatures and frequencies.

2.2 Structural Response. Choosing an appropriate set of shape functions to prescribe the structural deformation in Eq. (1) is of paramount importance toward enforcing an accurate low-order structural response. Depending on the choice of shape functions, a relatively small number of mode shapes can be utilized to describe the deformation. A series of candidate mode shapes is obtained by performing a modal analysis of the structure with the aid of a finite element method. The specific procedure to downselect candidate mode shapes differs depending on the application case of interest and will be discussed in the results section. For the purpose of the following discussion, a subset of suitable mode shapes is assumed to be selected.

The kinetic energy of the structure is defined as

$$T = \frac{1}{2} \int_{\Omega} \rho_m \|\dot{u}\|^2 d\Omega \quad (3)$$

Expanding this expression for a general multi-mode approximation allows the kinetic energy to be written solely in terms of integrals of the modal shape functions and generalized coordinates as

$$T = \frac{1}{2} \sum_i \sum_j \dot{q}_i \dot{q}_j \int_{\Omega} \rho_m (\vec{\psi}_i \cdot \vec{\psi}_j) d\Omega \quad (4)$$

The strain energy of the structure is expressed in terms of the double dot product of the stress and strain tensors as

$$U = \frac{1}{2} \int_{\Omega} \sum_r \sum_s \sigma_{rs} \epsilon_{rs} d\Omega \quad (5)$$

The deformations and materials of interest to this work are linear and isotropic, and so the strain energy may be written fully in terms of the strains [28]. The strain energy is then defined as

$$U = \frac{1}{2} \int_{\Omega} \lambda \left(\sum_r \epsilon_{rr} \right)^2 d\Omega + \int_{\Omega} \mu \sum_r \sum_s \epsilon_{rs} \epsilon_{rs} d\Omega \quad (6)$$

Expanding the strains in terms of the prescribed structural response described by Eq. (1) allows for the strain energy to be computed fully in terms of integrals of derivatives of the modal shape functions and the generalized coordinates as

$$U = \frac{1}{2} \int_{\Omega} \lambda \left(\sum_r \sum_k q_k \frac{\partial \psi_{k,r}}{\partial x_r} \right)^2 d\Omega + \frac{1}{4} \int_{\Omega} \mu \sum_r \sum_s \left(\sum_k q_k \left(\frac{\partial \psi_{k,r}}{\partial x_s} + \frac{\partial \psi_{k,s}}{\partial x_r} \right) \right) \cdot \left(\sum_l q_l \left(\frac{\partial \psi_{l,r}}{\partial x_s} + \frac{\partial \psi_{l,s}}{\partial x_r} \right) \right) d\Omega \quad (7)$$

2.3 Fluid Response. Computation of the virtual work term on the right-hand side of Eq. (2) is determined by the response of the surrounding fluid to the deformation of the structure. For the fluid–structural configurations considered in this research, the unsteady work is assumed to be dominated by pressure forces. Viscous forces are assumed to be negligible as the normal traction is substantially larger than the tangential traction. The virtual work

term is thus computed [29] as

$$\delta W = \sum_j \delta q_j \int_S -p' \hat{n} \cdot \vec{\psi}_j dS \quad (8)$$

The local piston theory of Zhang et al. [30] is utilized to model the unsteady pressure fluctuations that arise in response to the deformation of the structure. This aerodynamic model is a modified version of piston theory [31] where the local unsteady pressure fluctuation is computed in conjunction with representative steady aerodynamic data obtained from computational fluid dynamic (CFD) simulations of the flow configuration. The method in which the fluid computation is carried out varies for each fluid–structural configuration considered in this work; for now, it is assumed that a suitable flow solution has been obtained. The unsteady pressure fluctuation predicted by local piston theory is then

$$\begin{aligned} p' &= \rho_l a_l w \\ w &= \vec{v}_i \cdot \delta \hat{n} + \vec{v}_b \cdot \hat{n} \\ \delta \hat{n} &= \hat{n}_0 - \hat{n} \end{aligned} \quad (9)$$

where we note that the local surface velocity vector, \vec{v}_b , is directly informed by the prescribed structural deformation and is written as

$$\vec{v}_b = \dot{u} = \sum_j \dot{q}_j \vec{\psi}_j \quad (10)$$

Inserting the unsteady pressure fluctuation into Eq. (8) results in a surface integral that quantifies the virtual work performed upon the structure by unsteady aerodynamic forces. The right-hand side of Eq. (2) is now written as

$$\frac{d(\delta W)}{d(\delta q_j)} = - \int_S \rho_l a_l (\vec{v}_i \cdot \delta \hat{n}) (\hat{n} \cdot \vec{\psi}_j) dS - \sum_i \dot{q}_i \int_S \rho_l a_l (\vec{\psi}_j \cdot \hat{n}) (\hat{n} \cdot \vec{\psi}_i) dS \quad (11)$$

2.4 Governing Equations. The reduced structural and fluid response procedures quantify all terms of Eq. (2) in terms of known modal shape functions and steady aerodynamic data. The resulting equations are a nonlinear system of second-order, ordinary differential equations governing the generalized coordinates. The nonlinear governing equation for the i th generalized coordinate is written as

$$\sum_j T_{ij} \ddot{q}_j + \sum_j U_{ij} \dot{q}_j = F_i(\vec{q}) + \sum_j G_{ij}(\vec{q}) \dot{q}_j \quad (12)$$

where the resulting energy coefficients and fluid forcing functions are defined as

$$\begin{aligned} T_{ij} &= \int_{\Omega} \rho_m (\vec{\psi}_i \cdot \vec{\psi}_j) d\Omega \\ U_{ij} &= \int_{\Omega} \lambda \left(\sum_r \frac{\partial \psi_{i,r}}{\partial x_r} \right) \left(\sum_r \frac{\partial \psi_{j,r}}{\partial x_r} \right) d\Omega \\ &\quad + \frac{1}{2} \int_{\Omega} \left(\sum_r \sum_s \left(\frac{\partial \psi_{i,r}}{\partial x_s} + \frac{\partial \psi_{i,s}}{\partial x_r} \right) \right) \cdot \left(\sum_r \sum_s \left(\frac{\partial \psi_{j,r}}{\partial x_s} + \frac{\partial \psi_{j,s}}{\partial x_r} \right) \right) d\Omega \\ F_i &= - \int_S \rho_l a_l (\vec{v}_i \cdot \delta \hat{n}) (\hat{n} \cdot \vec{\psi}_i) dS \\ G_{ij} &= - \int_S \rho_l a_l (\vec{\psi}_i \cdot \hat{n}) (\hat{n} \cdot \vec{\psi}_j) dS \end{aligned} \quad (13)$$

The stability of the fluid–structural configuration is identified by first linearizing the governing equations about a steady equilibrium

state. The set of generalized coordinates is thus written as

$$q_j = q_j^e + q_j' \quad (14)$$

where q_j^e is the equilibrium state and q_j' is the perturbation state of the j th generalized coordinate. The equilibrium state is physically realized as the undeformed structural configuration, for which the full set of generalized coordinates is identically zero and as such $q_j^e = 0$ with all temporal derivatives of this state also being identically zero. The linearization is performed by expanding the nonlinear expressions associated with the unsteady fluid response, F_i and G_{ij} , about the equilibrium state using a Taylor series. The linearized governing equations for the i th perturbation quantity are

$$\sum_j T_{ij} \ddot{q}_j' - \sum_j G_{ij}(\bar{q}^e) \dot{q}_j' + \sum_j \left(U_{ij} - \frac{\partial F_i}{\partial q_j} \Big|_{\bar{q}=\bar{q}^e} \right) q_j' = 0 \quad (15)$$

where the final remaining fluid expression describing the linearized system is

$$\frac{\partial F_i}{\partial q_j} = - \int_S \rho_f a_i \left(\left(\vec{v}_l \cdot - \frac{\partial \hat{n}}{\partial q_j} \right) (\hat{n} \cdot \vec{w}_i) + (\vec{v}_l \cdot \delta \hat{n}) \left(\frac{\partial \hat{n}}{\partial q_j} \cdot \vec{w}_i \right) \right) dS \quad (16)$$

The underlying stability of the fluid–structural system depends directly on the stability of the perturbation quantities. The stability of the linearized system governing the perturbation is identified by imposing a harmonic ansatz as the solution to the perturbation [29], in the form

$$q_j' = \bar{q}_j e^{rt} \quad (17)$$

The linear system defined in Eq. (15) may be expressed as an eigenvalue problem of the form $\mathbf{A}\bar{q} = \bar{0}$ following the imposition of the harmonic ansatz. Solutions to the angular frequency, r , are acquired from the non-trivial solution acquired when $\det \mathbf{A} = 0$. If any of the angular frequency solutions have a positive real part, the linear system is unstable, and as such the fluid–structural configuration as a whole is unstable and is predicted to encounter aeroelastic flutter.

When considering radial turbomachines, the susceptibility of the device to forced response may be predicted by considering the damping ratio of the mode shape considered as the reduced structural response. For a single degree-of-freedom (SDOF) model, the damping ratio is defined as

$$\zeta = \frac{-G_{11}}{2\sqrt{T_{11} \cdot \left(U_{11} - (\partial F_1 / \partial q_1) \Big|_{\bar{q}^e} \right)}} \quad (18)$$

When comparing the equations of motion deduced from several different structural or fluid conditions of interest, the condition with lower modal damping ratio will exhibit a larger response magnitude at resonance than a condition with higher modal damping ratio. The relative response magnitude may then be used to diagnose which condition is more susceptible to forced response.

2.5 Numerical Implementation. Conducting the assessment of a given fluid–structural configuration involves computing the energy coefficients, T_{ij} and U_{ij} , and the fluid forcing functions, $\partial F_i / \partial q_j$ and G_{ij} . The energy coefficients, previously defined in Eq. (13), require the calculation of volume integrals of numerical solution data over the structural domain. These integrals are approximated numerically by re-writing the volume integral about the structural domain as a sum of volume integrals performed within the volume elements utilized to discretize the domain for the modal analysis calculation. These element-based integrals are then approximated using a quadrature rule. A four-point quadrature rule was selected to ensure that the numerical integration is of third-order accuracy, as this is the highest order of accuracy that

can be obtained from the use of second-order elements [32]. The volume integrals were therefore approximated as

$$\int_{\Omega} I d\Omega \approx \sum_{k=1}^{N_e} \sum_{l=1}^4 \alpha_l I_k(\vec{x}_l) |\mathbf{J}(\vec{x}_l)| \quad (19)$$

where N_e is the number of elements used to discretize the structural domain, I refers to the integrand considered in the approximation, $|\mathbf{J}(\vec{x}_l)|$ is the determinant of the Jacobian of the element evaluated at the integration location, and α_l and \vec{x}_l are the quadrature weights and locations, respectively.

The fluid forcing functions are defined by surface integrals about part or all of the surface bounding the structural domain. These integrals are approximated numerically in a manner that mirrors that of the volume integrals. The surface integral about the fluid–structural interface is first re-written as a sum of surface integrals about the element faces making up the interface. An element-wise surface integration is then performed using a three-point rule for triangular surfaces [33]. The surface integration procedure may be expressed mathematically as

$$\int_S I dS \approx \sum_{k=1}^{N_f} \sum_{l=1}^3 \beta_l I_k(\vec{x}_l) |\bar{\mathbf{J}}(\vec{x}_l)| \quad (20)$$

where N_f is the number of element faces used to discretize the fluid–structural interface, $|\bar{\mathbf{J}}(\vec{x}_l)|$ refers to the determinant of the two-dimensional Jacobian at the surface integration point, and β_l and \vec{x}_l refer to the weights and locations for surface quadrature.

The final remaining numerical procedure involves computing the surface unit normals and their derivatives. These quantities may vary about the position on the tetrahedral face as the quadratic tetrahedral surfaces may be curved. As the instantaneous deformation of the element surfaces may be defined in terms of the numerical shape functions and the original structural geometry, the unit normal may be computed in a numerical context at second-order accuracy and its derivative may be computed in a numerical context at first-order accuracy. All of the integration procedures have been numerically implemented and the validation of the implementation has been previously discussed in Ref. [7].

3 Results and Discussion

The modeling method has been applied to two different fluid–structural configurations. The method was first utilized to examine a classical panel flutter scenario that has been extensively studied both numerically and experimentally in the past. This study was performed to verify the capability of the method to predict the onset of aeroelastic flutter in a scenario where the instability is known to arise. The method was then utilized to verify the stability

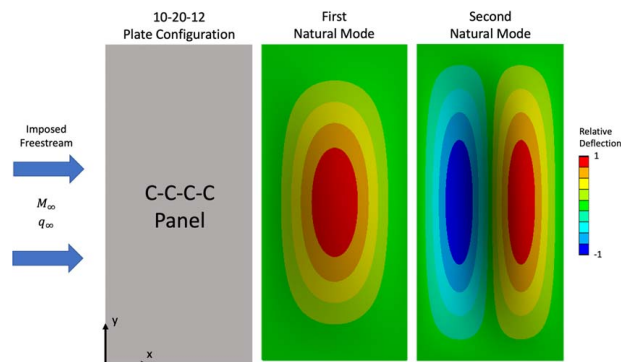


Fig. 1 Fluid–structural panel flutter configuration considered (left) and mode shapes utilized to prescribe reduced structural response (right). The flutter response is composed equally of the first and second natural mode shapes [36].

and damping characteristics of a high-pressure radial turbine wheel. That study was performed to assess the usefulness of the method in identifying the aeroelastic behavior of radial turbines. The same turbine wheel was further studied experimentally in an effort to validate the findings of the modeling method.

3.1 Panel Flutter. The reduced-order modeling method was applied to the “10-20-12” rectangular panel configuration previously studied by Dowell and Voss [34]. The fluid–structural configuration is described in Fig. 1. In this scenario, a thin structural panel is installed in a wind tunnel and clamped on all four sides to a rigid frame. The panel is exposed on one side to a supersonic freestream flow, and exposed on the other side to a cavity of unperturbed air. This case was considered at a variety of freestream Mach numbers with the intent of acquiring an independent prediction of the flutter boundary.

3.1.1 Structural Response. The natural mode shapes of the structure were obtained by performing a modal analysis of the rectangular panel. The modal analysis was performed using a finite element method contained within the ANSYS Mechanical Enterprise v19.2 [35] suite. The structural mesh of the panel was discretized utilizing second-order tetrahedra. A high resolution mesh of 4,209,645 nodes and 2,097,012 elements was constructed to ensure that the elements were of acceptable skewness and quality. This mesh was further deemed acceptable as it is of improved resolution over the meshes considered in Ref. [7], where mesh resolution studies were performed to ensure accurate computation of the coefficients and forcing functions needed for stability computations.

Previous discussions of rectangular panel flutter [36] with aspect ratios identical to the structural panel considered in this study indicate that the flutter response is composed of the first two natural mode shapes with nodal lines extending along the spanwise direction of the panel. Consequently, a two-mode approximation composed of these two modes is necessary to predict the onset of aeroelastic flutter with this modeling method. These two mode shapes, pictured in Fig. 1, were computed as part of the modal analysis and were supplied to the modeling tool.

3.1.2 Fluid Response. Modeling the reduced fluid response of a flat, rectangular plate is trivial. No numerical simulations were needed as the local piston theory anticipates the use of steady, Euler solution data. Therefore, the local fluid quantities furnished to the local piston theory to compute the unsteady pressure loading are equivalent to the freestream flow quantities. Mirroring the procedure performed by Dowell and Voss, the freestream Mach number and dynamic pressure are imposed for each flow scenario considered. These quantities fully define the relevant piston theory flow quantity, $\rho_\infty a_\infty U_\infty$, and no additional information is required to compute the unsteady pressure fluctuation.

The theory developed by Dowell and Voss [34] to predict the onset of panel flutter utilized a modified, quasi-static version of piston theory where the influence of surface motion about its mean position is neglected. Only the influence of the misalignment of the local steady flow velocity with respect to the deformed surface orientation is considered in their aerodynamic model. To provide a meaningful comparison of theory, this study matched the aerodynamic theory by enforcing a quasi-static version of local piston theory in which all $G_{ij} = 0$.

3.1.3 Discussion. Stability predictions were obtained by first computing the kinetic and strain energy coefficients of the rectangular panel with the prescribed structural deformation. A sweep of fluid conditions was then performed by first imposing the freestream Mach number and then slowly increasing the freestream dynamic pressure. For each Mach number and dynamic pressure combination, the method was used to assess the stability of the fluid–structural configuration. The dynamic pressure was no longer varied once the fluid–structural configuration was assessed to be unstable, indicating the onset of flutter. The next Mach

number of interest was then imposed and the process was repeated. The resulting flutter boundary predicted by the modeling method developed in this work was compared against the theoretically computed flutter boundary and experimentally observed flutter band presented by Dowell and Voss. The dynamic pressure at which the onset of flutter occurs is difficult to quantify during experiment and instead a “flutter band” of dynamic pressures is presented between which the true dynamic pressure associated with the onset of flutter lies (detailed discussion of the identification of this band is presented in Ref. [34]). The comparison of flutter boundaries is depicted in Fig. 2.

The flutter boundary computed by the reduced-order model compares favorably to the theoretically predicted flutter boundary of Dowell and Voss as well as the flutter band those authors observed experimentally. The deviations in theoretically predicted flutter boundaries exist for several reasons. The first lies in the prescribed structural response. The theory of Dowell and Voss imposed a structural response composed of mode shapes approximated utilizing a Rayleigh–Ritz method, which are an approximation of the true panel natural modes. The modeling method considered in this work computed the mode shapes utilizing a numerical method, and as such the imposed structural deformation more closely approximates the true flutter response.

The second deviation between the theory of Dowell and Voss and the theory derived in this work lies in the approximate fluid response. While both theories utilize piston theory to predict the response of the fluid to the deformation of the structure, the leading term of the piston theory employed by Dowell and Voss has been augmented by a factor of $M/\sqrt{M^2 - 1}$ to improve the predictions of the pressure fluctuations in the low-supersonic flow regime. This modification accounts for the discrepancies in slope present at the lower-end of the flow regime, but will have a negligible impact for larger Mach numbers.

The final difference between the referenced theory and the modeling method discussed in this research concerns the influence of the air cavity that exists beneath the rectangular panel. The presence of the cavity was identified by Dowell and Voss to have a substantial effect on the flutter response [34]. The theory employed by the authors was modified to account for the influence of the cavity on the flutter boundary. Augmenting the Euler–Lagrange model with a term to account for the pressure fluctuation due to volume changes in the cavity, such as that of Ventres and Dowell [37], has been seen to lower the discrepancy between both theory predictions, although exact comparisons cannot be made as the fluid density and temperature in the cavity are not available in the comparison literature.

3.2 Turbocharger Turbine. The modeling method was next applied to the high-pressure turbine (HPT) wheel within a wastegate-less, dual-stage turbocharger designed by Danielson Aircraft Systems. The geometry of the high-pressure turbine wheels is

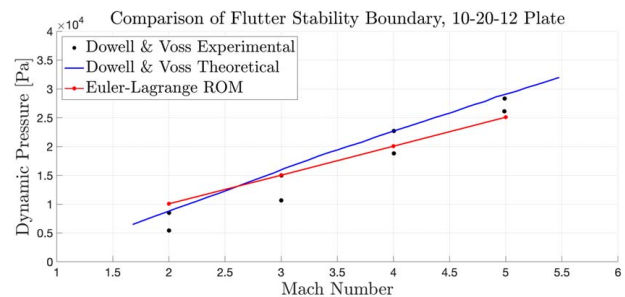


Fig. 2 Panel flutter stability boundary as determined by Euler–Lagrange derived reduced-order model from this work (solid line with scatter point), theory of Dowell and Voss (solid line without scatter point), and experiments performed by Dowell and Voss (scatter points)

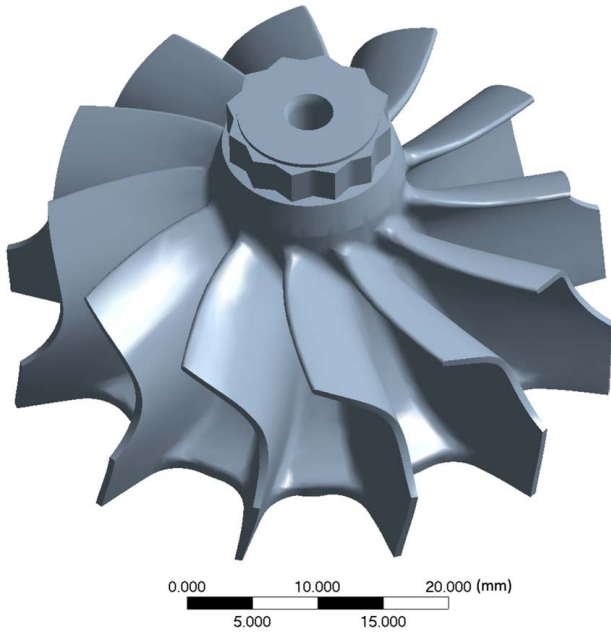


Fig. 3 Geometry of the high-pressure turbine wheel considered in this study

depicted in Fig. 3. The turbine wheel was first operated in an experimental setting to identify conditions at which substantial blade deformations, indicating the presence of a fluid–structural interaction, were measured. These conditions were then investigated with the modeling method to ascertain the ability of the model to predict the susceptibility of the turbine wheel to the onset of aeroelastic flutter or forced response at the problematic conditions.

3.2.1 Experimental Analysis. An experimental investigation of the turbocharger was performed at the Army Research Laboratory (ARL) in order to identify the true dynamic behavior of the high-pressure turbine wheel during device operation. In these experiments, the turbocharger was installed in the Small Engine Altitude Research Facility (SmEARF). The SmEARF is an altitude chamber engine cell that is capable of simulating altitude conditions up to 25,000 feet [38]. A process flow diagram of the SmEARF is depicted in Fig. 4.

While installed in the altitude chamber, the turbine blade deflections were obtained using a non-intrusive stress measurement system (NSMS) developed by Agilis. Four probes were mounted circumferentially around each turbine wheel. A light source is transmitted by each probe to illuminate the tips of the turbine blades. The reflected light is then sensed by a photodetector to track the instant in time at which the blade tip passes the probe. The recorded

blade tip arrivals can then be used to identify the blade tip deflection [39]. Additional information describing the dynamic response, such as blade damping ratio, can also be computed in conjunction with the experimental data and blade tip deflection measurements [40].

Experimental analysis of the turbocharger was performed at a wide variety of operating points associated with small aircraft flight conditions. The NSMS identified substantial turbine blade tip deflections at a subset of these operating points, indicating the potential onset of an aeroelastic event. Groups of turbine blades were observed to be excited at slightly different turbopool rotational speeds during each event. This mistuning phenomenon is a consequence of manufacturing tolerances and may be used to associate the structural response during each event with different, albeit unknown, mode shapes. An example of this categorization is provided in the example abstracted blade waterfall plot displayed in Fig. 5.

The NSMS measurements indicate that during each aeroelastic event, the same blade mistuning pattern is present in each turbine wheel. The presence of identical blade dynamic responses indicate that the same mode shape is being excited during each aeroelastic event. However, additional information such as the nodal diameters present during the response and the spatial distribution of displacement associated with the mode shape cannot be identified.

For each condition, the resonant response was characterized on a blade-by-blade basis. For each blade, a curve fit of a SDOF model is performed about 100 amplitude data points [41]. The SDOF model assumes that each blade acts as a single mass-spring-damper with no coupling between other blades of the turbine wheel. A sinusoidal forcing function with constant amplitude is assumed across the resonant response, with the forcing frequency assumed to be changing slowly enough that the steady-state solution is dominant. The major output of the SDOF model procedure is a damping ratio associated with the blade dynamic response. The blade-based damping ratios are output by the Agilis software as a bar chart, with each bar color-coded with respect to how well the SDOF model fits the experimental data in a least-squares sense. The damping ratios as computed for the same example experimental condition associated with the previous blade waterfall plot are depicted in Fig. 6.

An additional output of the SDOF model procedure performed by the Agilis software is an identification of the engine order (EO) associated with the resonant response. For the high-pressure turbine wheel, the response is associated with forcing frequencies indicative of engine orders lesser than the number of blades making up the respective turbine wheel. Resonances at these low engine orders have been previously identified as being associated with excitations of the first-order bending or torsional mode shapes that are driven by the loss of circular symmetry present in radial devices [42,43].

3.2.2 Structural Response. The dual-stage turbocharger studied in this work is intended for operation within an aircraft over a variety of altitudes and rotational speeds. The turbine

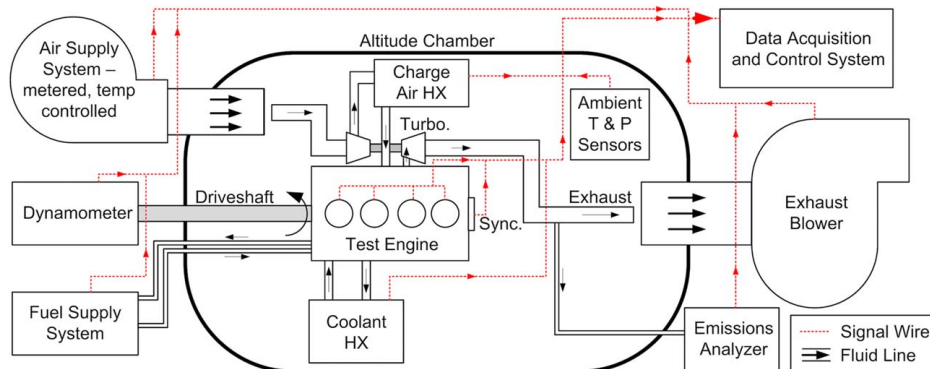


Fig. 4 SmEARF process flow diagram, adapted from Ref. [38]

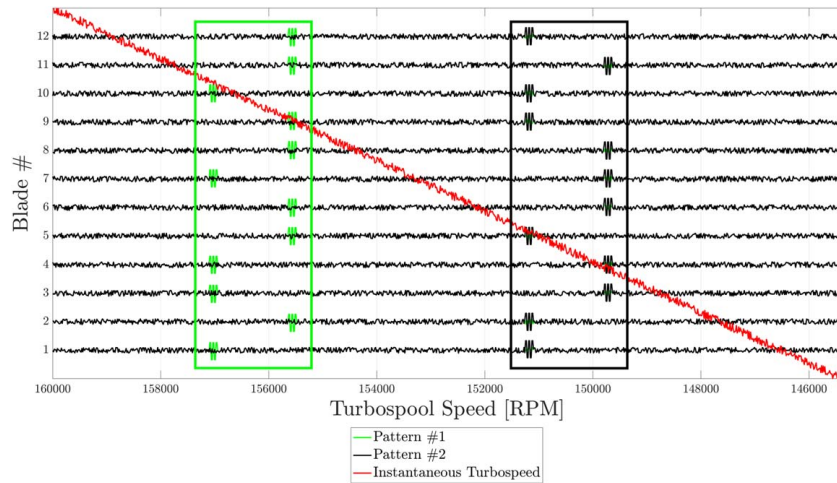


Fig. 5 Example blade waterfall plot of the high-pressure turbine. Deformation of each blade is plotted as a function of turbospool speed (horizontal lines), with turbospool rotation history overlaid (diagonal line). The rectangles indicate the effect of blade mistuning on the resonant response.

wheel structure will be influenced by rotational speed through the effects of centripetal stress-stiffening and spin softening. While the natural mode shapes obtained from a modal analysis of the structure are not impacted significantly by variations in rotational speed, the corresponding natural frequencies can be changed.

Structural meshes were first constructed for the high-pressure turbine to conduct the modal analyses. The turbine is discretized by second-order tetrahedral elements and the resulting mesh is composed of 221,473 nodes and 142,581 elements. The characteristic side lengths of the second-order tetrahedral elements ranged from 0.1 mm to 1 mm. A mesh refinement study was performed to ensure that this mesh would be suitable for accurately computing the natural mode shapes and associated natural frequencies to be considered in this work. Five different meshes were considered in the study. The natural frequencies of the first bending and torsional mode shapes were tracked. The mesh discussed above was selected as the best choice between mesh resolution and accuracy. The difference in natural frequencies with respect to the chosen mesh are provided in Table 1.

Modal analyses were then conducted over a parametric sweep of turbospool rotational speeds at in vacuo conditions. Five rotational conditions were considered, spanning from the rest state up to the maximum rotational speed measured during preliminary engine

tests of the turbocharger. Each modal analysis was conducted using the ABAQUS [44] software suite. The turbine wheel is composed of Inconel, and the material properties of the wheel were set assuming that the structure was operating in an environment temperature equal to the maximum exhaust gas temperature. While the structure is not expected to encounter this temperature over all operating conditions of interest, the choice of maximum exhaust gas temperature was selected to obtain a conservative estimate of the structural stiffness. The turbine wheel was fixed at the bearing location and the remainder of the wheel was left unconstrained.

The modal analysis procedure results in a series of natural mode shapes. These mode shapes are classified into bending modes and torsional modes based on the behavior of the deformation. As discussed earlier in Sec. 3.2.1, the first-order bending and torsional mode shapes of the high-pressure turbine are of particular interest for the numerical analyses to be considered. These mode shapes are shown in Fig. 7.

Once computed, the natural frequencies of the mode shapes of the high-pressure turbine wheel were tracked as a function of rotational speed. A Campbell diagram of the turbine wheel was constructed by plotting the natural frequencies as a function of rotational speed and overlaying the engine orders associated with the turbospool rotational speed. The full diagram with higher-order mode shapes is provided alongside a locally magnified region about which the experiments were performed. This diagram is displayed in Fig. 8. The scatter points on the diagrams denote conditions at which the experiments identified substantial blade deflections associated with the presence of a fluid-structural interaction. As the experimental apparatus is unable to identify the specific mode being excited, scatter points are applied to intersections associated with both the first bending and torsional mode shape. The coloring of

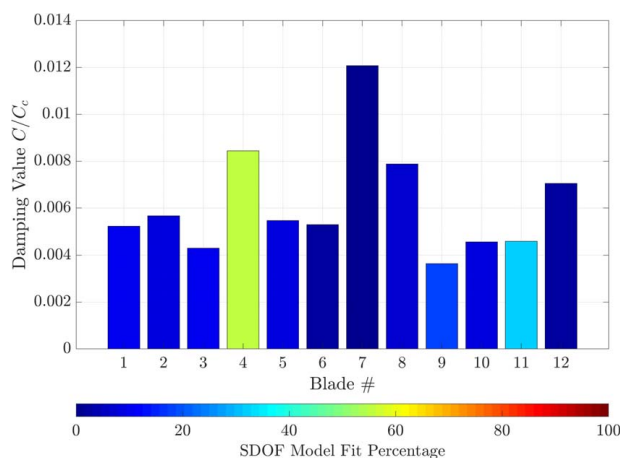


Fig. 6 Bar plot of critical damping ratio for each high-pressure turbine blade at an example operating condition. Each bar is color-coded by SDOF model fit percentage.

Table 1 Difference in first bending mode and first torsional mode natural frequencies with respect to natural frequencies obtained from selected mesh

Maximum element size (mm)	First bending mode frequency (% difference)	First torsional mode frequency (% difference)
0.6	-0.10	-0.11
0.8	-0.04	-0.05
1.0	0.00	0.00
1.5	0.13	0.13
2	0.56	0.57

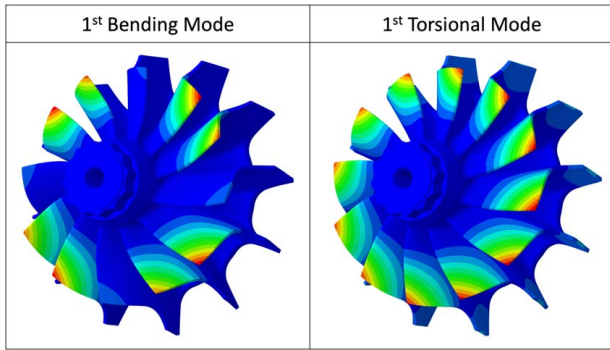


Fig. 7 First bending and torsional mode shape of the high-pressure turbine wheel. Larger total deformation is exhibited at the blade tips.

the scatter points is associated with the colorbar and denotes the modal damping as identified from the model framework. A more thorough discussion of the predictions is provided later in this section.

Previous investigations of turbomachine blade deformation have observed that blade deformations can generally be composed of multiple natural mode shapes [45]. The onset of coupled-mode response in these devices has been correlated to mass ratio and natural frequency separation [46]. The turbine wheel considered in this study is of large material-to-fluid mass ratio and exhibits large natural frequency separation between different-order bending and torsional modes, implying that a coupled-mode response is not of concern to the device in consideration. Therefore, a single-mode approximation of the structural response is sufficient for this study and at each potential resonance condition of interest, the associated natural mode shape was used to prescribe the reduced structural response.

3.2.3 Fluid Response. The aerodynamic data used to inform the local piston theory were obtained by performing a steady CFD simulation of the full dual-stage turbocharger geometry. The numerical simulations were performed with the ANSYS CFX v19.2 [47] suite that utilizes an element-based finite volume method (EbFVM). The EbFVM first discretizes the fluid domain into a series of elements whose centroids are used to construct the finite volumes in which the governing equations are discretized and solved. The element shape functions are then used to interpolate the solution within the fluid domain.

In the majority of the flow domain, the steady Reynolds-averaged Navier–Stokes (RANS) equations are solved with a $k-\epsilon$ turbulence model with scalable wall functions. This turbulence model was chosen as a consequence of its previous success in acquiring the flow solution within a turbocharger [26]. While other turbulence

models, namely, the $k-\omega$ shear stress transport model, have been successfully utilized [48] to obtain the flow solution, and no substantial influence on the flow solution has been observed in preliminary investigations of the choice of turbulence model performed as part of this work. In the subdomains surrounding the turbine blades, the RANS equations are augmented with centripetal and Coriolis source terms to model the effect of the turbine blade rotation on the flow without physically rotating the blades.

A frozen rotor technique is applied at the interface of the turbine blade subdomains and the remainder of the computational domain to enforce continuity of the pressure and absolute velocity components. Previous investigations of applying the frozen rotor technique to turbocharger flow configurations have found that the inlet and outlet flow quantities do not vary significantly in comparison to a fully developed transient simulation [49], and as such the flow solution obtained from this technique is considered to be a valid approximation to the true flow field exhibited during device operation. To ensure that the specific orientation of the turbine rotors would not strongly impact the solution, a sensitivity study was performed at the operating condition associated with the largest high-pressure turbine rotational speed. The study considered four different turbine rotor orientations, including a condition at which a turbine blade was aligned with the volute tongue. The studies identified that the rotor orientation impacted the maximum and minimum static temperature, pressure, and density by less than 2% of the orientation imposed in this work. The frozen rotor technique was deemed an acceptable solution method by these metrics.

The discretization scheme of the CFD solver and the specific choice of inlet and outlet port boundary conditions were informed following the work of Galindo et al. [50]. The advective terms of the RANS equations were discretized using a second-order upwind scheme that blends to first-order when flux limited [47]. The total temperature, mass flowrate, and turbulence intensity are imposed equally at the three intake manifold ports, and the static pressure and turbulence intensity are imposed at the outlet. As mentioned previously, the local piston theory utilized to predict the unsteady pressure loading anticipates the use of Euler solution data. However, the ANSYS CFX solver is unable to solve the steady Euler equations and the accuracy and validity of an Euler solution in this flow configuration are unknown. As a compromise, free-slip conditions are imposed at all solid domain boundaries to mimic an Euler solution. Consequently, the fluid viscosity was allowed to vary and was computed as a function of temperature through the use of Sutherland’s law. The fluid thermal conductivity was also allowed to vary and was modeled utilizing kinetic theory [51].

The mesh used to acquire the flow solution within the domain was constructed using linear tetrahedral elements. A mesh convergence study was performed to ensure that a converged flow solution was acquired. Two meshes were considered; the first was composed of 508,709 nodes and 2,630,550 elements, while the second was composed of 1,229,049 nodes and 6,529,235 elements. The flow

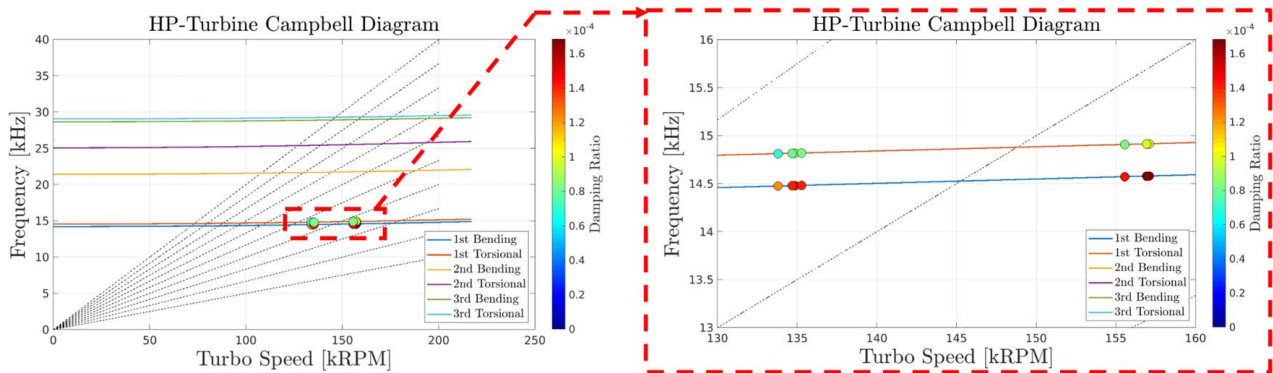


Fig. 8 Campbell diagram of the high-pressure turbine (left), with magnified region showcasing damping ratio predictions from a single-mode approximated system at operating conditions associated with aeroelastic events (right)

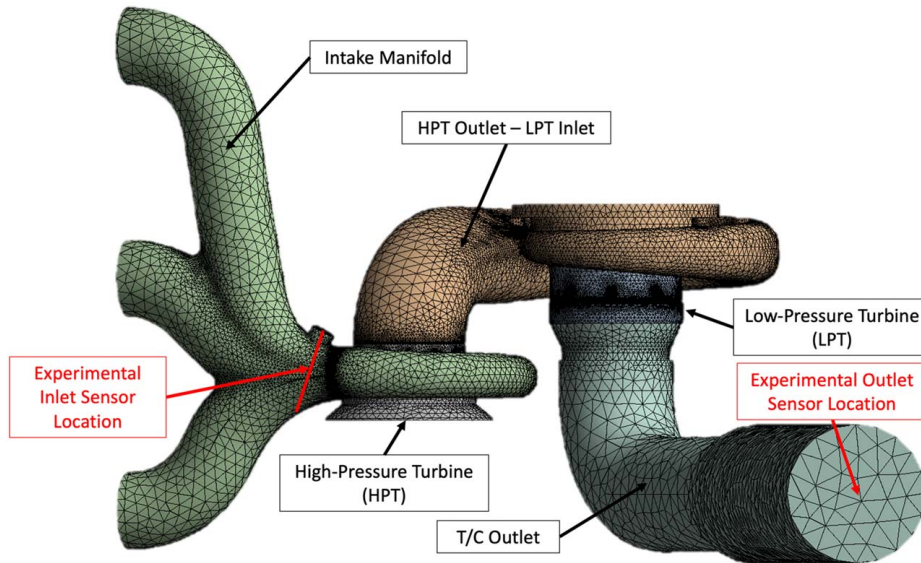


Fig. 9 Mesh of the turbocharger (T/C) computational domain with computational subdomains and experimental sensor locations identified by in-figure text

solution at one representative operating condition was then computed on both meshes. Convergence was first assessed by comparing the numerically predicted inlet static pressure and outlet total temperature against measurements taken at these locations experimentally. The comparisons showed that the predicted flow solution quantities changed negligibly between the two meshes. Additionally, both meshes predicted both the inlet static pressure and outlet total temperature to within 10% of the experimentally observed quantities. Convergence was next assessed by comparing the force coefficients on the high- and low-pressure turbine wheels. The coefficients were found to change by less than 2% between both meshes. These facts indicated that the flow solution was sufficiently converged, and the more refined of the two meshes was used as the mesh on which to compute the steady flow solution for use within the modeling method. The mesh used to obtain the flow solution, along with the locations of the experimental sensors, is depicted in Fig. 9.

In addition, a validation campaign was conducted at ARL in which 30 operating conditions were observed. During each condition, the static pressure and total temperature were measured at the inlet sensor and the total temperature, only, was measured at the outlet sensors. The sensor locations correspond to the same

locations labeled in Fig. 9. The full quantitative results are omitted for brevity but the analysis identified that the inlet quantities are generally predicted to within 5% of the experimental counterparts, while the outlet total temperature is predicted globally to within 15% of the experimental measurement. These predictions were deemed to be acceptable in context of the approximation techniques utilized to obtain the flow solution.

Once a flow solution was acquired, the static pressure, density, and velocity components in the rotating frame of reference were extracted on the fluid-structural interface of the turbine wheel from the solver. These quantities comprise the representative, steady flow solution to be utilized by the local piston theory in order to approximate the unsteady pressure fluctuation that develops on the interface as the structure deforms. Example pressure and density fields as extracted on the high-pressure turbine at operation as installed on an aircraft at 5000 feet with onboard engine operating at 2500 rotations per minute are displayed in Figs. 10 and 11, respectively.

For each operating condition of interest, a CFD simulation needs to be performed in order to obtain the flow solution over the high-pressure turbine blades. These simulations were performed at a variety of operating conditions and altitudes that ARL considered

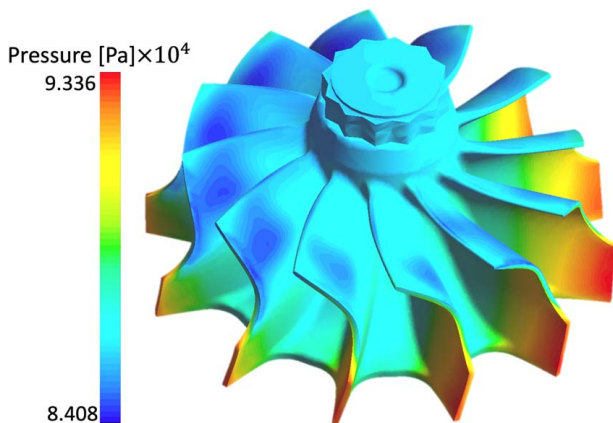


Fig. 10 Pressure field solution on high-pressure turbine as computed from 5000 foot altitude, 2500 RPM engine operation

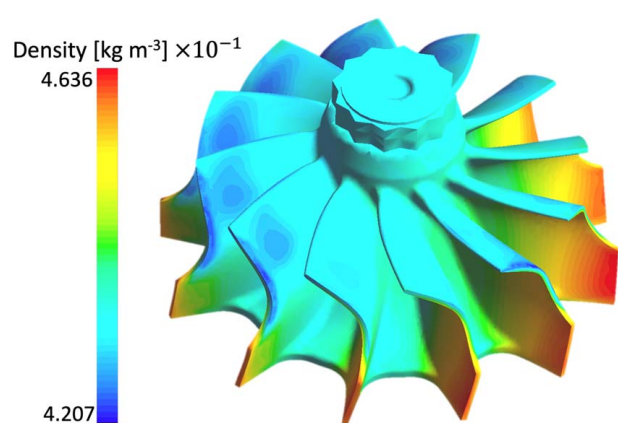


Fig. 11 Density field solution on high-pressure turbine as computed from 5000 foot altitude, 2500 RPM engine operation

Table 2 Comparison of damping ratios for high-pressure turbine conditions as observed experimentally by NSMS and as predicted numerically by the modeling method

Experiment num.	EO excited	HPT rot. speed	Exp. SDOF fit percentage	Exp. max damping	Exp. min damping	Exp. avg damping	Model predicted damping	
							First bending	First torsional
1	6E	157,084	68	9.80×10^{-4}	5.00×10^{-4}	6.00×10^{-4}	1.66×10^{-4}	9.63×10^{-5}
2	7E	134,879	82	1.55×10^{-3}	5.20×10^{-4}	8.80×10^{-4}	1.46×10^{-4}	8.52×10^{-5}
3	6E	156,920	52	1.51×10^{-3}	5.00×10^{-4}	8.40×10^{-4}	1.68×10^{-4}	9.79×10^{-5}
4	6E	155,548	48	1.51×10^{-3}	5.00×10^{-4}	7.60×10^{-4}	1.44×10^{-4}	8.35×10^{-5}
5	7E	134,682	93	9.20×10^{-4}	5.00×10^{-4}	6.20×10^{-4}	1.40×10^{-4}	8.15×10^{-5}
6	7E	133,802	42	1.05×10^{-3}	5.60×10^{-4}	7.60×10^{-4}	1.22×10^{-4}	7.08×10^{-5}
7	8E	135,270	93	9.30×10^{-4}	5.00×10^{-4}	6.20×10^{-4}	1.40×10^{-4}	8.17×10^{-5}

to be of interest. Each simulation was performed with boundary conditions quantified from experimental measurements obtained at ARL during preliminary investigations of the turbocharger at the conditions of interest. For most applications of the reduced-order model, experimental data will not already exist and as such alternative methods must be used to estimate the inlet and outlet boundary conditions.

3.2.4 Dynamics Prediction. For each condition of interest, the linearized governing equations obtained from application of the modeling method were used to obtain a numerical prediction regarding the dynamic response of the turbine wheel. The metric utilized to represent the dynamic response was the damping ratio associated with the response of a single degree-of-freedom system, defined in Eq. (18).

The local piston theory utilized in this study is a homogeneous aerodynamic forcing theory that is unable to predict an unsteady pressure fluctuation when the structure is undeformed. As such, the method cannot be used to strictly predict the onset of forced response, but identifying operating conditions where the system damping ratio is low presents an alternative method from which to identify the susceptibility of the configuration to large resonant vibrations as well as to ascertain its aeroelastic stability. If the damping ratio is negative, the system exhibits aeroelastic flutter. For situations where the damping ratio is positive, conditions with smaller damping ratios are identified as conditions where the system is most susceptible to large resonant vibrations.

The damping ratio was computed for the high-pressure turbine wheel at all operating conditions associated with an aeroelastic event as identified by experiment. The computed damping ratios were then overlaid on the device Campbell diagram, as displayed in Fig. 8.

3.2.5 Discussion. The high-pressure turbine wheel only exhibited an aeroelastic event during transient operation of the turbocharger. For each aeroelastic event, a representative operating condition was obtained by temporally averaging the measured flow quantities needed to perform a CFD simulation over the time period during which the aeroelastic event was observed. These representative operating conditions denote a set of boundary conditions required to obtain a flow solution that is furnished to the modeling tool in order to determine the modal damping ratio associated with each natural mode shape. In an attempt to compare the numerical predictions to the experimental observations, the operating conditions associated with each aeroelastic event were furnished to the modeling tool to predict the modal damping ratio associated with deformation in the first bending and torsional mode of the high-pressure turbine. The comparisons of numerical damping ratio to experimentally observed damping ratio data are provided in Table 2.

Two immediate conclusions may be drawn from the comparisons of the numerical predictions to the experimental observations. First, at all operating conditions considered for the high-pressure turbine, the damping ratio predicted by the modeling tool is strictly positive.

This indicates that the turbine wheel is stable over all operating points and the turbine wheel never encounters a flutter phenomenon. This is an observation that has additionally been confirmed from observations made during the experiments performed at ARL. This is an encouraging sign showcasing potential utility of the modeling framework. However, to fully validate the ability of the model to predict flutter, additional studies must be performed on a device that is observed to encounter the instability during experiment. These studies are recommended as future work.

The numerical predictions of the modal damping ratio are additionally identified to be within an order of magnitude of the experimentally deduced blade damping ratios. This finding is especially encouraging when considered in the context of the multitude of simplifications used to keep the numerical expense of the modeling method to a minimum. However, while the magnitude comparisons lend some trust to the numerical predictions, it is important to note that the numerically predicted modal damping ratio cannot be directly compared to the experimentally deduced blade damping ratios. The damping ratio associated with the numerical prediction is obtained with the full turbine wheel structure in the context of structural response in a single-mode shape, whereas the damping ratio associated with the experiment is obtained on a blade-by-blade basis and deduced from a single degree-of-freedom approximation of the true deformation. These fundamental differences preclude direct, one-to-one comparisons of the presented damping ratios.

4 Summary and Conclusions

A reduced-order model capable of determining the aeroelastic response of a fluid–structural configuration has been developed. The model computes the aeroelastic response using uncoupled simulation data and differs from other models in that it leverages a modified form of piston theory to approximate the unsteady pressure fluctuation associated with structural deformation, with steady CFD data as the single input needed to compute the reduced fluid response. The modeling method has been demonstrated to reliably determine the onset of flutter as compared against experimental observations from both classical panel flutter configurations and a radial compact turbine. The damping characteristics of the radial compact turbine deforming in its first-order bending and torsional modes were compared against blade-based damping ratio observations obtained from a non-intrusive stress measurement system. However, shortcomings associated with the limited ability of the current experimental state-of-the-art to faithfully capture the full dynamic behavior of high-speed turbomachinery limit the utility of the damping comparison. These shortcomings are identified as important obstacles that must be overcome in order to further the validation of reduced-order numerical methodologies.

Acknowledgment

Research was sponsored by the Army Research Laboratory and was accomplished under Cooperative Agreement Number

W911NF-19-2-0077. The views and conclusions contained in this document are those of the authors and should not be interpreted as representing the official policies, either expressed or implied, of the Army Research Laboratory or the U.S. Government. The U.S. Government is authorized to reproduce and distribute reprints for Government purposes notwithstanding any copyright notation herein.

This work was supported in part by high-performance computer time and resources from the DoD High Performance Computing Modernization Program.

The authors gratefully thank Danielson Aircraft Systems for sharing the geometry of the radial turbomachine analyzed as part of this work.

Conflict of Interest

There are no conflicts of interest.

Data Availability Statement

The datasets generated and supporting the findings of this article are obtainable from the corresponding author upon reasonable request.

Nomenclature

a	= speed of sound
\hat{n}	= deformed surface unit normal
p	= fluid static pressure
q	= generalized coordinate
r	= frequency of harmonic response
t	= time
\vec{u}	= structural deformation vector
\vec{v}	= velocity vector
w	= fluid downwash
\vec{x}	= position vector
I	= integrand of a specified volume or surface integral
S	= bounding surface of structure
T	= kinetic energy
U	= strain energy
W	= virtual work
\mathbf{A}	= fluctuation quantity coefficient matrix
\mathbf{J}	= Jacobian
\hat{n}_0	= undeformed surface unit normal
N_e	= number of elements used to discretize structural domain
N_f	= number of element faces used to discretize fluid–structural interface
N_m	= number of modes prescribing deformation
x, y, z	= coordinate directions
F, G	= aerodynamic forcing functions
α	= quadrature weights of volume integration
β	= quadrature weights of surface integration
ϵ	= strain
ζ	= system damping ratio
λ	= material Lamé’s constant
μ	= material shear modulus
ρ	= density
σ	= stress
Ω	= structural domain
$\vec{\psi}$	= structural deformation modal shape function

Subscripts

1, 2, 3	= component indices
b	= local position on the surface
i, j, k, r, s	= dummy indices
l	= local fluid quantity
m	= material quantity

Superscript

e = equilibrium quantity

Operators

δ = virtual operator, displacement vector between deformed and undeformed surface unit normals
 $\dot{(\)}$ = temporal derivative
 $\bar{(\)}$ = initial condition of fluctuation quantity
 $'$ = fluctuation

References

- [1] McGowan, R. C., Pieri, J. J., Szedlmayer, M. T., Kim, K., Clerkin, P. J., Kruger, K. M., Gondol, D., et al., 2019, “Experimental Vibration Analysis of an Aircraft Diesel Engine Turbocharger,” AIAA Propulsion and Energy 2019 Forum, Indianapolis, IN, Aug. 19–22, American Institute of Aeronautics and Astronautics, pp. 4008–4025.
- [2] McGowan, R. C., Murugan, M., Szedlmayer, M. T., Kim, K. S., Kruger, K. M., Gondol, D. J., Kweon, C.-B. M., et al., 2019, “Structural Dynamics and Aeroelasticity of Airborne Diesel Engine Turbochargers,” Turbo Expo: Turbomachinery Technical Conference and Exposition, Phoenix, AZ, June 17–21, American Society of Mechanical Engineers, p. V008T26A024.
- [3] Mansouri, H., and Ommi, F., 2019, “Performance Prediction of Aircraft Gasoline Turbocharged Engine at High-Altitudes,” *Appl. Therm. Eng.*, **156**, pp. 587–596.
- [4] Bents, D. J., Mockler, T., Maldonado, J., and Schmitz, P. C., 1998, “Propulsion System for Very High Altitude Subsonic Unmanned Aircraft,” *SAE Trans.*, **107**, pp. 100–115.
- [5] Rozenkranc, M., and Ernst, J., 2003, “Tactical UAV Engines Integration in IAI,” 2nd AIAA ‘Unmanned Unlimited’ Conference and Workshop & Exhibit, San Diego, CA, Sept. 15–18, American Institute of Aeronautics and Astronautics, pp. 6534–6543.
- [6] Luongo, A., Nuccio, P., and Vignoli, M., 2006, “Optimization of a Light Aircraft Spark-Ignition Engine,” Tech. Rep., SAE Technical Paper No. 2006-01-2420.
- [7] Fellows, D. W., Bodony, D. J., and McGowan, R. C., 2021, “Reduced-Order Modeling of Extreme Speed Turbochargers,” Turbo Expo: Power for Land, Sea, and Air, Vol. 84997, Virtual, Online, June 7–11, American Society of Mechanical Engineers, p. V006T19A002.
- [8] Dang, K., Wiersma, H., Meininger, R., Gibson, J., Kim, K., and Szedlmayer, M., 2018, “High Cycle Fatigue Assessment of a Diesel Engine Turbocharger,” AHS International 74th Annual Forum & Technology Display, Phoenix, AZ, May 14–17, American Helicopter Society.
- [9] Hodges, D. H., and Pierce, G. A., 2011, *Introduction to Structural Dynamics and Aeroelasticity*, Vol. 15, Cambridge University Press, New York.
- [10] Lubomski, J. F., 1980, “Status of NASA Full-Scale Engine Aeroelasticity Research,” Tech. Rep., NASA Technical Memorandum 81500.
- [11] Vogt, D., 2005, “Experimental Investigation of Three-Dimensional Mechanisms in Low Pressure Turbine Blades,” PhD thesis, KTH Royal Institute of Technology, Stockholm.
- [12] Nowinski, M., and Panovsky, J., 1999, “Flutter Mechanisms in Low Pressure Turbine Blades,” *ASME J. Eng. Gas Turbines Power*, **122**(1), pp. 82–88.
- [13] Waite, J. J., and Kielb, R. E., 2014, “Physical Understanding and Sensitivities of Low Pressure Turbine Flutter,” *ASME J. Eng. Gas Turbines Power*, **137**(1), p. 012502.
- [14] Hoyniak, D., and Fleeter, S., 1986, “Forced Response Analysis of an Aerodynamically Detuned Supersonic Turbomachine Rotor,” *ASME J. Vib. Acoust. Stress Reliab. Des.*, **108**(2), pp. 117–124.
- [15] Kielb, J. J., Abhari, R. S., and Dunn, M. G., 2001, “Experimental and Numerical Study of Forced Response in a Full-Scale Rotating Turbine,” Turbo Expo: Power for Land, Sea, and Air, New Orleans, LA, June 4–7, American Society of Mechanical Engineers, p. V004T03A029.
- [16] Gao, Y., Gutierrez Salas, M., Petrie-Repar, P., and Gezork, T., 2019, “Forced Response Analysis of a Radial Turbine With Different Modelling Methods,” Turbo Expo: Turbomachinery Technical Conference and Exposition, Phoenix, AZ, June 17–21, American Society of Mechanical Engineers, p. V07AT36A022.
- [17] Kawakubo, T., 2010, “Unsteady Rotor–Stator Interaction of a Radial-Inflow Turbine With Variable Nozzle Vanes,” Turbo Expo: Power for Land, Sea, and Air, Vol. 44021, Glasgow, UK, June 14–18, American Society of Mechanical Engineers, pp. 2075–2084.
- [18] Heuer, T., Gugau, M., Klein, A., and Ansel, P., 2008, “An Analytical Approach to Support High Cycle Fatigue Validation for Turbocharger Turbine Stages,” Turbo Expo: Power for Land, Sea, and Air, Berlin, Germany, June 9–13, American Society of Mechanical Engineers, pp. 723–732.
- [19] Chiang, H.-W. D., and Kielb, R. E., 1993, “An Analysis System for Blade Forced Response,” *ASME J. Turbomach.*, **115**(4), pp. 762–770.
- [20] Kammerer, A., and Abhari, R. S., 2008, “Experimental Study on Impeller Blade Vibration During Resonance—Part II: Blade Damping,” *ASME J. Eng. Gas Turbines Power*, **131**(2), p. 022509.
- [21] Kammerer, A., and Abhari, R. S., 2008, “Experimental Study on Impeller Blade Vibration During Resonance—Part I: Blade Vibration Due to Inlet Flow Distortion,” *ASME J. Eng. Gas Turbines Power*, **131**(2), p. 022508.
- [22] Bréard, C., Vahdati, M., Sayma, A., and Imregun, M., 2000, “An Integrated Time-Domain Aeroelasticity Model for the Prediction of Fan Forced Response Due to Inlet Distortion,” *J. Eng. Gas Turbines Power*, **124**(1), pp. 196–208.

- [23] Vahdati, M., and Imregun, M., 1996, "A Non-linear Aeroelasticity Analysis of a Fan Blade Using Unstructured Dynamic Meshes," *IMEchE J. Mech. Eng. Sci.*, **210**(6), pp. 549–564.
- [24] Green, J., and Marshall, J., 1999, "Forced Response Prediction Within the Design Process," 3rd European Conference on Turbomachinery, London, UK, Mar. 2–5, Institution of Mechanical Engineers, IMEHE Paper C557/1121/99.
- [25] Moffatt, S., Ning, W., Li, Y., Wells, R. G., and He, L., 2005, "Blade Forced Response Prediction for Industrial Gas Turbines," *J. Propul. Power*, **21**(4), pp. 707–714.
- [26] Dickmann, H.-P., Secall Wimmel, T., Szwedowicz, J., Filsinger, D., and Roduner, C. H., 2005, "Unsteady Flow in a Turbocharger Centrifugal Compressor: Three-Dimensional Computational Fluid Dynamics Simulation and Numerical and Experimental Analysis of Impeller Blade Vibration," *ASME J. Turbomach.*, **128**(3), pp. 455–465.
- [27] Goldstein, H., Poole, C. P., and Safko, J. L., 2002, *Classical Mechanics*, Addison-Wesley Press, San Francisco, CA.
- [28] Sadd, M. H., 2009, *Elasticity: Theory, Applications, and Numerics*, Academic Press, Burlington, MA.
- [29] Dowell, E. H., Curtiss, H. C., Scanlan, R. H., and Sisto, F., 1989, *A Modern Course in Aeroelasticity*, Vol. 3, Springer, New York.
- [30] Zhang, W. W., Ye, Z. Y., Zhang, C. A., and Liu, F., 2009, "Supersonic Flutter Analysis Based on a Local Piston Theory," *AIAA J.*, **47**(10), pp. 2321–2328.
- [31] Meijer, M.-C., and Dala, L., 2016, "Generalized Formulation and Review of Piston Theory for Airfoils," *AIAA J.*, **54**(1), pp. 17–27.
- [32] Zienkiewicz, O. C., Taylor, R. L., and Zhu, J. Z., 2005, *The Finite Element Method*, Butterworth-Heinemann, Oxford.
- [33] Dhatt, G., Lefrançois, E., and Touzot, G., 2012, *Finite Element Method*, John Wiley & Sons, Hoboken, NJ.
- [34] Dowell, E. H., and Voss, H. M., 1965, "Theoretical and Experimental Panel Flutter Studies in the Mach Number Range 1.0 to 5.0," *AIAA J.*, **3**(12), pp. 2292–2304.
- [35] ANSYS Inc., 2019, "ANSYS Mechanical User Guide."
- [36] Dowell, E. H., 1970, "Panel Flutter—A Review of the Aeroelastic Stability of Plates and Shells," *AIAA J.*, **8**(3), pp. 385–399.
- [37] Ventres, C., and Dowell, E., 1970, "Comparison of Theory and Experiment for Nonlinear Flutter of Loaded Plates," *AIAA J.*, **8**(11), pp. 2022–2030.
- [38] Szedlmayer, M. T., Kim, K., Kweon, C.-B., and Kruger, K., 2017, "The Effect of Fuel Aromatic Content and Cetane Number on Combustion in a UAV Diesel Engine," 53rd AIAA/SAE/ASEE Joint Propulsion Conference, Atlanta, GA, July 10–12, American Institute of Aeronautics and Astronautics, p. 5029.
- [39] McGowan, R. C., Fellows, D. W., Bodony, D. J., Mojica, J. R., Pieri, J. J., Kweon, C.-B. M., Gibson, J. A., Meiningner, R. D., and Musser, M. R., 2020, "Effect of Altitude on Turbomachinery Vibration in an Aircraft Compression-Ignition Engine," Turbo Expo: Turbomachinery Technical Conference and Exposition, Virtual, Online, Sept. 21–25, American Society of Mechanical Engineers, p. V008T20A022.
- [40] Agilis Measurement Systems, Inc., 2017, "Blade Vibration Measurement."
- [41] Washburn, R., 2021, "Private Communication."
- [42] Bréard, C., Green, J., and Imregun, M., 2003, "Low-Engine-Order Excitation Mechanisms in Axial-Flow Turbomachinery," *J. Propul. Power*, **19**(4), pp. 704–712.
- [43] Elliott, R., Sayma, A., and Imregun, M., 2005, "Aeromechanical Design of Damped High Pressure Turbine Blades Subject to Low Engine Order Forcing," Tech. Rep., Rolls-Royce Ltd, Derby.
- [44] Dassault Systèmes Simulia Corporation, 2019, "ABAQUS, Version 2019."
- [45] Schuff, M., and Chenaux, V. A., 2021, "Coupled Mode Flutter Analysis of Turbomachinery Blades Using an Adaptation of the p - k Method," *ASME J. Eng. Gas Turbines Power*, **143**(2), p. 021017.
- [46] Clark, S., 2010, "Coupled-Mode Flutter for Advanced Turbofans," Master's thesis, Duke University, Durham, NC.
- [47] ANSYS Inc., 2019, "ANSYS CFX Theory Reference."
- [48] Galindo, J., Hoyas, S., Fajardo, P., and Navarro, R., 2013, "Set-Up Analysis and Optimization of CFD Simulations for Radial Turbines," *Eng. Appl. Comput. Fluid Mech.*, **7**(4), pp. 441–460.
- [49] Fellows, D. W., Bodony, D. J., and McGowan, R. C., 2021, "Reduced-Order Modeling of Aeroelasticity in Extreme Speed Turbochargers," AIAA Propulsion and Energy 2021 Forum, Virtual, Aug. 9–11, American Institute of Aeronautics and Astronautics, pp. 3466–3480.
- [50] Galindo, J., Fajardo, P., Navarro, R., and García-Cuevas, L. M., 2013, "Characterization of a Radial Turbocharger Turbine in Pulsating Flow by Means of CFD and Its Application to Engine Modeling," *Appl. Energy*, **103**, pp. 116–127.
- [51] ANSYS Inc., 2019, "ANSYS Fluent User Guide."